Suppelementary Material for "Shape Analysis of Euclidean Curves under Frenet-Serret Framework"

Perrine Chassat[1]
[1]LaMME, University of Paris-Saclay
perrine.chassat@univ-evry.fr

Juhyun Park[1,2]
[2]ENSIIE, Evry
juhyun.park@ensiie.fr

Nicolas Brunel[1,2,3]
[3]Quantmetry, Paris
nicolas.brunel@ensiie.fr

Abstract

This supplementary material contains additional proofs of the propositions, detailed explanations of the method based on the Frenet-Serret framework, and additional results on the experiments conducted in the main article. The code used to obtain these experimental results is also provided with this document.

1. Additional Proofs

Proposition 1 (Proposition 3 of section 4.3 in the main article)**.** *Let $\theta \in \mathcal{H}$, we have*

$$\|A_\theta(s(t))\|_F = \|\theta(s(t))\|_2 \,. \tag{1}$$

Proof. We recall that the vector $\theta(s) = (\theta_1(s), \dots, \theta_{d-1}(s))$ is a $(d-1)$-dimensional vector of $\mathbb{R}$. The matrix $A_\theta(s)$ is skew-symmetric with the superdiagonal equal to $-\theta(s)$, the subdiagonal equal to $\theta(s)$, and all the other coefficients null.

$$\|A_\theta(s(t))\|_F^2 = \frac{1}{2}\text{tr}\left(A_\theta(s)^T A_\theta(s)\right) = -\frac{1}{2}\text{tr}\left(A_\theta(s)^2\right) = -\frac{1}{2}\sum_{i=1}^{d}\sum_{j=1}^{d} a(s)_{ij}a(s)_{ji} \,.$$

We differentiate three cases depending on i:

$$\begin{cases} \text{if } i = 1: & \sum_{j=1}^{d} a(s)_{1,j}a(s)_{j,1} = a(s)_{1,2}a(s)_{2,1} = -\theta_1(s)^2 \\ \text{if } i = d: & \sum_{j=1}^{d} a(s)_{d,j}a(s)_{j,d} = a(s)_{d,d-1}a(s)_{d-1,d} = -\theta_{d-1}(s)^2 \\ \text{otherwise:} & \sum_{j=1}^{d} a(s)_{i,j}a(s)_{j,i} = a(s)_{i,i-1}a(s)_{i-1,i} + a(s)_{i,i+1}a(s)_{i+1,i} = -\theta_{i-1}(s)^2 - \theta_i(s)^2 \end{cases}$$

and then we have,

$$\begin{aligned} \|A_\theta(s(t))\|_F^2 &= -\frac{1}{2}\sum_{i=1}^{d}\sum_{j=1}^{d} a(s)_{ij}a(s)_{ji} = \frac{1}{2}\sum_{i=2}^{d-1}\theta_{i-1}(s)^2 + \frac{1}{2}\theta_{d-1}(s)^2 + \frac{1}{2}\sum_{i=2}^{d-1}\theta_i(s)^2 + \frac{1}{2}\theta_1(s)^2 \\ &= \sum_{i=1}^{d-1}\theta_i(s)^2 = \theta(s)^T\theta(s) = \|\theta(s)\|_2^2 \,. \end{aligned}$$

□

Proposition 2 (Proposition 5 of section 4.3 in the main article)**.** *The metric on $F([0,1], \mathbb{R}^d)$ induced by the Riemannian metric on $\Psi([0,1]) \times \mathcal{C}$ defined by $d_{SRC} := d_\Psi \oplus d_\mathcal{C}$ is invariant under the action of Diff$_+$([0,1]).*

Proof. Let $h \in \text{Diff}_+([0,1])$, $x_0, x_1 \in F([0,1], \mathbb{R}^d)$ with $(\sqrt{\dot{s}_0},\, c_0), (\sqrt{\dot{s}_1},\, c_1) \in \Psi([0,1]) \times \mathcal{C}$ their corresponding square-root curvature transform. Under this representation the induced distance on $F([0,1], \mathbb{R}^d)$ is

$$d_{\text{SRC}}(x_0 \circ h, x_1 \circ h) = d_\Psi(\sqrt{\dot{s}_0} * h, \sqrt{\dot{s}_1} * h) + d_\mathcal{C}(c_0 * h, c_1 * h) \,.$$

Let us show that the action of $\mathrm{Diff}_+([0,1])$ on $\Psi([0,1])$ and on $\mathcal{C}$ is by isometry with respect to the $\mathbb{L}^2$ metric. For $\Psi([0,1])$ we have

$$\left\langle \sqrt{\dot{s}_0} * h, \sqrt{\dot{s}_1} * h \right\rangle = \int_0^1 \left\langle \sqrt{\dot{s}_0(h(t))\dot{h}(t)}, \sqrt{\dot{s}_1(h(t))\dot{h}(t)} \right\rangle dt = \int_0^1 \left\langle \sqrt{\dot{s}_0(u)}, \sqrt{\dot{s}_1(u)} \right\rangle du\,, \quad u = h(t)$$

and with the same change of variable, we have for $\mathcal{C}$,

$$\begin{aligned}
\|c_0 * h - c_1 * h\|^2_{\mathbb{L}^2} &= \int_0^1 \left| \sqrt{\dot{h}(t)}\sqrt{\dot{s}_0(h(t))} \frac{\theta_0(s_0(h(t)))}{\sqrt{\|\theta_0(s_0(h(t)))\|}} - \sqrt{\dot{h}(t)}\sqrt{\dot{s}_1(h(t))} \frac{\theta_1(s_1(h(t)))}{\sqrt{\|\theta_1(s_1(h(t)))\|}} \right|_2 dt \\
&= \int_0^1 \left| \sqrt{\dot{s}_0(u)} \frac{\theta_0(s_0(u))}{\sqrt{\|\theta_0(s_0(u))\|}} - \sqrt{\dot{s}_1(u)} \frac{\theta_1(s_1(u))}{\sqrt{\|\theta_1(s_1(u))\|}} \right|_2 du\,, \quad u = h(t) \\
&= \int_0^1 |c_0(u) - c_1(u)|_2 \, du\,.
\end{aligned}$$

Then d_{SRC} is invariant under the action of $\mathrm{Diff}_+([0,1])$

$$d_{\mathrm{SRC}}(x_0 \circ h, x_1 \circ h) = d_\Psi(\sqrt{\dot{s}_0} * h, \sqrt{\dot{s}_1} * h) + d_{\mathcal{C}}(c_0 * h, c_1 * h) = d_\Psi(\sqrt{\dot{s}_0}, \sqrt{\dot{s}_1}) + d_{\mathcal{C}}(c_0, c_1) = d_{\mathrm{SRC}}(x_0, x_1)\,.$$

□

2. Details on the curve representation $\mathcal{R}_Q$

We mention at the end of section 4.1 in the main article the idea of considering the following direct extension of the square-root velocity function of a curve $x \in F([0,1], \mathbb{R}^d)$ by its whole Frenet frame, suggested in [1],

$$\mathcal{R}_Q(x)(t) = \sqrt{\dot{s}(t)} Q(s(t))\,. \tag{2}$$

For all $t \in [0,1]$, $\mathcal{R}_Q(x)(t) \in \mathcal{GL}_d(\mathbb{R})$ and if we consider the Frobenius norm on $\mathcal{GL}_d(\mathbb{R})$, we have $\frac{1}{d}\|\mathcal{R}_Q(x)(t)\| = \sqrt{\dot{s}(t)}$, as $Q(s(t)) \in SO(d)$. Then the Euclidean curve x can be reconstructed from $\mathcal{R}_Q(x)$ by integration along the time variable of the first vector of $\frac{1}{d}\|\mathcal{R}_Q(x)(t)\|\mathcal{R}_Q(x)(t) = \dot{s}(t)Q(s(t))$.

The set of such mathematical representations $\mathcal{R}_Q$ is a subset of the set of measurable curves from $[0,1]$ to $\mathcal{GL}_d(\mathbb{R})$ such that the curve $t \mapsto \frac{\mathcal{R}_Q(x)(t)}{\frac{1}{d}\|\mathcal{R}_Q(x)(t)\|} = Q(s(t))$ is a Frenet path and therefore an element of $\mathcal{F}_0$. We recall here the definition of $\mathcal{F}_0$,

$$\mathcal{F}_0 = \left\{ Q \in \mathbb{L}^2\left([0,1], SO(d)\right) \,|\, Q'(s) = Q(s)A_\theta(s), Q(0) = I_d, \theta \in \mathcal{H} \right\}\,. \tag{3}$$

One could attempt to show that the set of representations $\mathcal{R}_Q$ is a manifold if the set of Frenet path $\mathcal{F}_0$ is one. However, we show from the Frobenius theorem that $\mathcal{F}_0$ is not a manifold.

The set $\mathcal{F}_0$ corresponds to the set of solutions of the first-order ordinary differential equations, with fixed initial conditions,

$$Q'(s) = X_\theta(Q(s))\,, \tag{4}$$

where X_θ is a vector field on the Lie group $SO(d)$, defined by $X_\theta(Q(s)) = Q(s)A_\theta(s)$ with $\theta \in \mathcal{H}$. We denote $\mathcal{D}$ the subbundle of the tangent bundle $TSO(d)$, defined by $\mathcal{D} = \mathrm{span}\{X_\theta \text{ for } \theta \in \mathcal{H}\}$. Then, the Frobenius theorem [3, 2] states that the subbundle $\mathcal{D}$ is involutive, and therefore integrable, if, for any two vector fields X^1_θ and X^2_θ of $\mathcal{D}$, the Lie bracket $[X^1_\theta, X^2_\theta]$ is also in $\mathcal{D}$. However, we have

$$[X^1_\theta, X^2_\theta](Q(s)) = X^1_\theta(X^2_\theta(Q(s))) - X^2_\theta(X^1_\theta(Q(s))) = Q(s)\left(A_{\theta^2}(s)A_{\theta^1}(s) - A_{\theta^1}(s)A_{\theta^2}(s)\right)$$

and we can show easily that the matrix $B = A_{\theta^2}(s)A_{\theta^1}(s) - A_{\theta^1}(s)A_{\theta^2}(s)$ no longer has the form a matrix A_θ with $\theta \in \mathcal{H}$. Indeed if we look at the coefficient $B_{i,i+2}$, for $1 < i < d-1$, we have

$$B_{i,i+2} = \sum_{j=1}^{d} a^1_{i,j} a^2_{j,i+2} = \theta^1_i \theta^2_{i+1}$$

which is not equal to zero a priori. Then $[X_\theta^1, X_\theta^2]$ does not take values in $\mathcal{D}$, and therefore $\mathcal{D}$ is not integrable. This means that $\mathcal{F}_0$, the set of integral curves defined from $\mathcal{D}$, is not a manifold. Given this last result and since we are looking, in this work, for a mathematical representation of a Euclidean curve that allows us to define a complete Riemannian framework for shape analysis (geodesic, distance, mean), the representation $\mathcal{R}_Q$ does not correspond, and that is why we have not considered it further.

3. Additional Results on Experiments

3.1. Experiments on synthetic curves *(section 5.2 of the main article)*

In the main article, we consider three types of synthetic curves analyzed in section 5.2: spirals in $\mathbb{R}^2$ (Figure 1), circular helices in $\mathbb{R}^3$ (Figure 2), and loops in $\mathbb{R}^2$ characterized by a curvature function shape with one large peak (Figure 3, 4, 5).

For each one, we propose in the article to visualize the geodesic paths under each method (SRVF, SRC, Frenet curvatures) between two particular curves chosen to have significantly different characteristics (significantly different numbers of spins for the two spirals and helices and peaks of curvature quite far apart for the two loops). We show in this supplementary material the results obtained by considering, for each type of curve, the geodesic path between two curves with slightly closer characteristics, and we display the evolution of the curvatures of the curves along the geodesic. Again, the three methods, SRVF, SRC, and Frenet curvatures, are compared each time. For the case of the loops, we propose in the article an experiment on a set of 20 randomly generated loops by picking a random position of the peak of curvatures between 0.1 and 0.9. From these random curves, we display in Figure 3 the matrices of pairwise distances computed using each of the three distances: SRVF, SRC, and Frenet curvatures. In this supplementary material, we show the results obtained by doing the same kind of experiment for the two other types of curves (spiral and helix). In addition, we add the plot of the 20 curves considered in each experiment and the Karcher means of these 20 curves computed from the three different methods.

The following results highlight that only the method based on the SRC representation of Euclidean curves allows to define a curve shape analysis framework having two important properties: being sufficiently "elastic" to avoid the occurrence of artefacts along the geodesic or in the mean (Section 3.1.1), and being consistent when analyzing a set of curves sharing a particular geometry (Section 3.1.1, 3.1.2 and 3.1.3).

3.1.1 Loop in $\mathbb{R}^2$

In Figures 4 and 5 of the main article, we see that the shapes of curves along the SRVF and the Frenet curvatures geodesic paths are not consistent with this particular type of curve. By considering two loops with peaks of curvature a bit closer, Figure S.1, this result remains true for the geodesic path under the Frenet curvatures representation. However, in that case, the curves along the SRVF geodesic path are more coherent; they still have one peak of curvature and not two, as in Figure 5. This important difference in the shape of the curves along the SRVF geodesic paths between the case of Figures 4 and 5 and the one of the Figure S.1 could be an explanation for the inconsistency visible in the SRVF heatmaps of Figure 3. The set of 20 curves considered to obtain the pairwise distance matrices of Figure 3 in the main article is shown in Figure S.2, and the Karcher means of this set, computed with each distance, are plotted on the right. We clearly see with this result that the Frenet curvature representation is not sufficient and that considering a representation that allows for registration of the points along the curve seems to be a more than necessary criterion to have a coherent shape analysis framework.

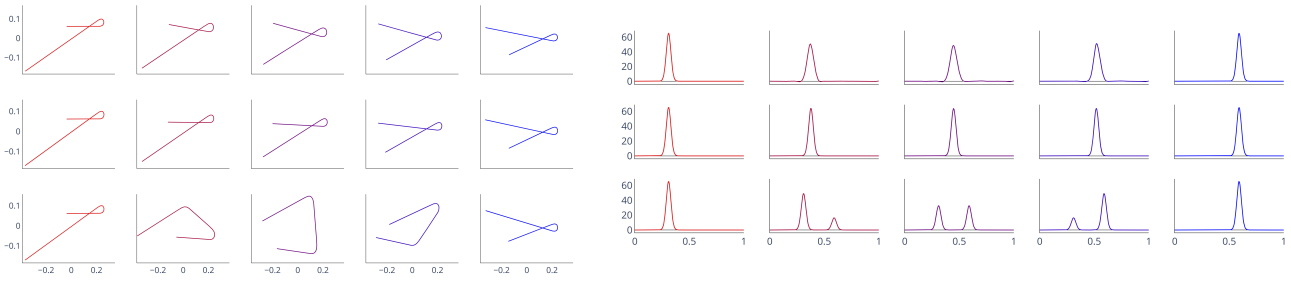

Figure S.1: Geodesic paths (left) between two loops with curvature peaks located at 0.31 and 0.59 and corresponding curvatures (right) of each curve along the geodesics: SRVF (1^{st} row), SRC (2^{nd} row), and Frenet curvatures (3^{rd} row).

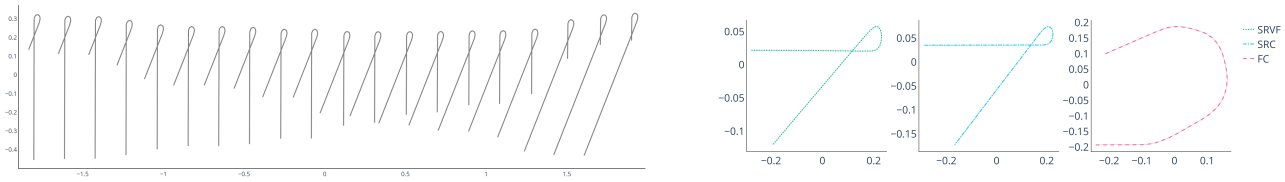

Figure S.2: Karcher means (right) computed under each method (SRVF, SRC, and Frenet curvatures) from a set of 20 loops, with random locations of curvature peak, plotted on the left (same set as the one used to compute the matrices of pairwise distances in Figure 3 of the main article).

3.1.2 Spiral in $\mathbb{R}^2$

Figure 1 of the main article shows the geodesic paths computed under the SRVF and the SRC framework between two spirals with a significantly different number of spins. This same result is shown here in Figure S.3 in which we also display the result obtained by using the Frenet curvatures representation and the corresponding evolution of the curvature along the geodesics for the three methods. As mentioned in the main article, in this case of spirals, the SRC and Frenet curvatures methods give really similar results. These spirals are generated with a curvature function in logarithm. As explained in the article, the curves along the SRVF geodesic are no longer spirals in the case of Figure S.3. They are more coherent along the SRVF geodesic in Figure S.4 between two spirals with a less different number of spins. However, the curvatures still show a peak at the end that is not present in the two considered curves. In both figures, we see that methods based on a representation using the Frenet curvatures are really more suitable and consistent in this case.

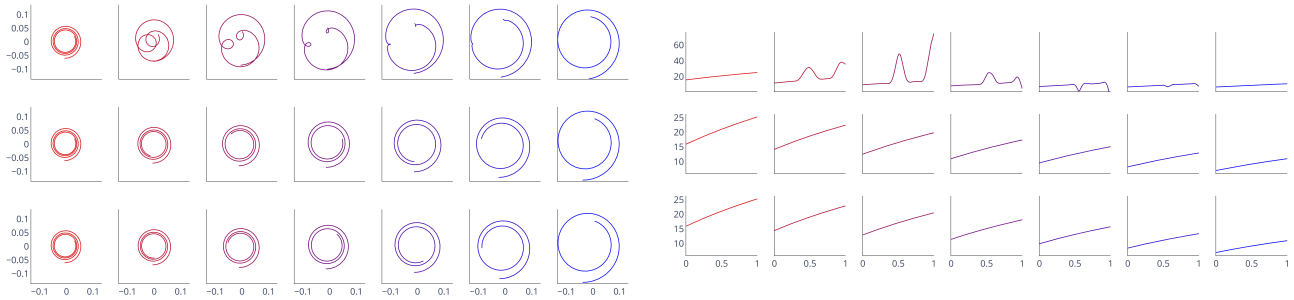

Figure S.3: Geodesic paths (left) between two spirals with a different number of spins and corresponding curvatures (right) of each curve along the geodesics: SRVF (1^{st} row), SRC (2^{nd} row), and Frenet curvatures (3^{rd} row).

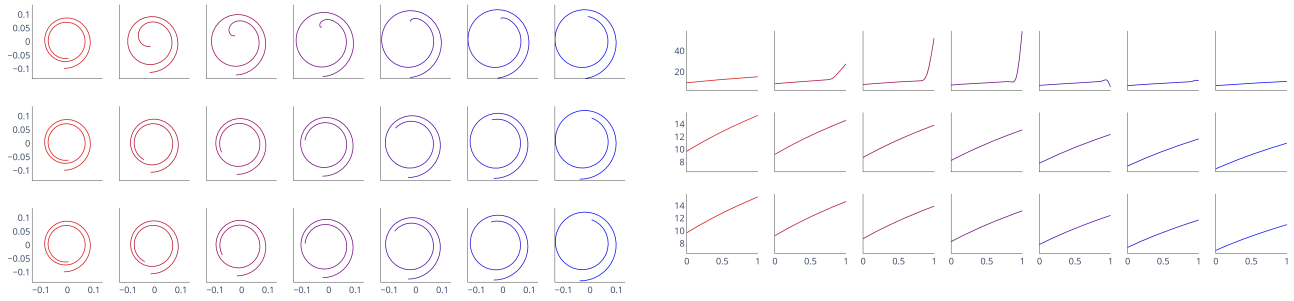

Figure S.4: Geodesic paths (left) between two spirals with a close number of spins and corresponding curvatures (right) of each curve along the geodesics: SRVF (1^{st} row), SRC (2^{nd} row), and Frenet curvatures (3^{rd} row).

We generate 20 spirals randomly from curvature functions defined by multiplying by a random number between 7 and 37 the function $t \mapsto \log(t+2)$. The results computed in this experiment are displayed in Figure S.5. The Karcher means summarize very well the previous analysis; the SRC and Frenet curvatures means are consistent with the set of curves considered, which is not the case for the SRVF one. The distance matrices show that the Frenet curvatures-based methods calculate distances globally close to zero within this set. They, therefore, seem to capture that there is a common geometry shared by the curves. This is less the case for the SRVF distance matrix, which seems to well partition the spirals according to the number of spins, but the distances are not always monotone as a function of the number of spins.

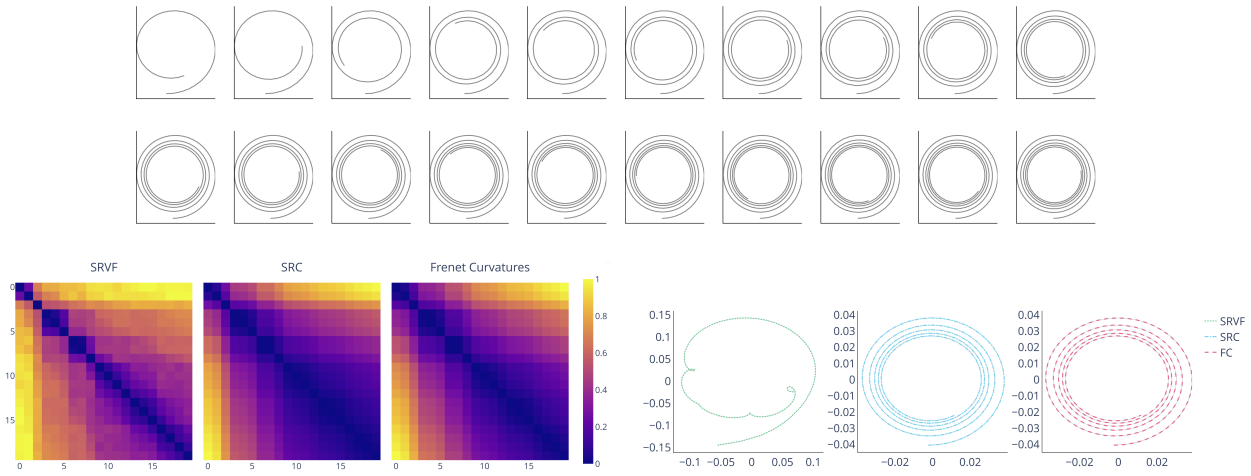

Figure S.5: Matrices of pairwise distances (right top) and Karcher means (right bottom) computed under each method (SRVF, SRC, and Frenet curvatures) from a set of 20 random spirals plotted on the left.

3.1.3 Circular helix in $\mathbb{R}^3$

The analysis and comparison of the three methods for spirals are almost identical in the case of the three-dimensional helices proposed in Figure 2 of the main article (Figure S.7 here). In that case, the 20 random circular helices, Figure S.8, are generated from a random number of spins, and there are all of unit length. We observe again that the SRVF framework is a bit more coherent between helices having a close number of spins in Figure S.6, but the Karcher mean is still inconsistent with the set of helices considered; it is no more a helix. Here also, in three-dimension, the Frenet curvatures-based methods define a shape analysis framework well adapted to this particular geometry.

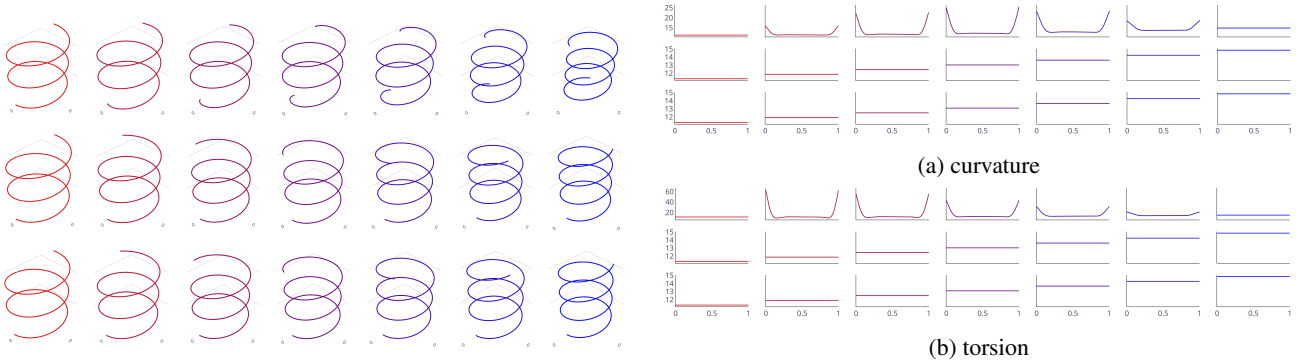

(a) curvature

(b) torsion

Figure S.6: Geodesic paths (left) between two circular helices in 3D with a close number of spins and corresponding curvatures (right) of each curve along the geodesics: SRVF (1^{st} row), SRC (2^{nd} row), and Frenet curvatures (3^{rd} row).

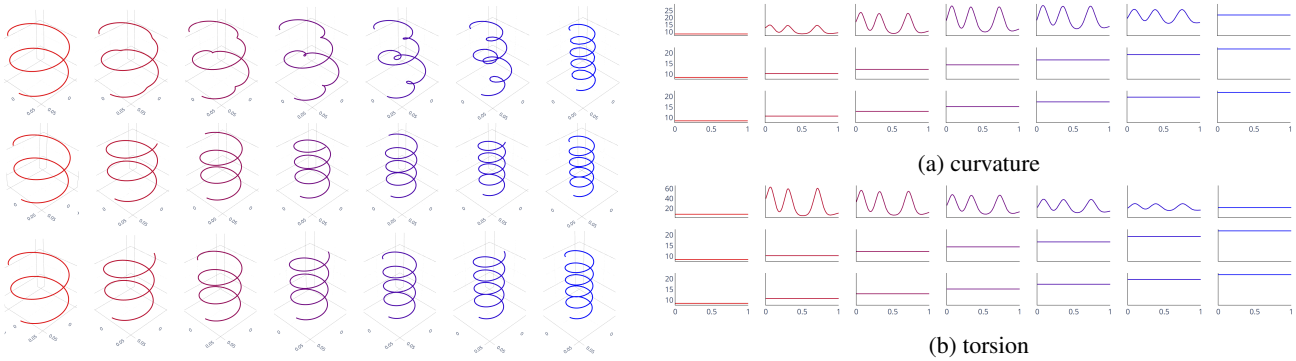

(a) curvature

(b) torsion

Figure S.7: Geodesic paths (left) between two circular helices with a different number of spins and corresponding curvatures (right) of each curve along the geodesics: SRVF (1^{st} row), SRC (2^{nd} row), and Frenet curvatures (3^{rd} row).

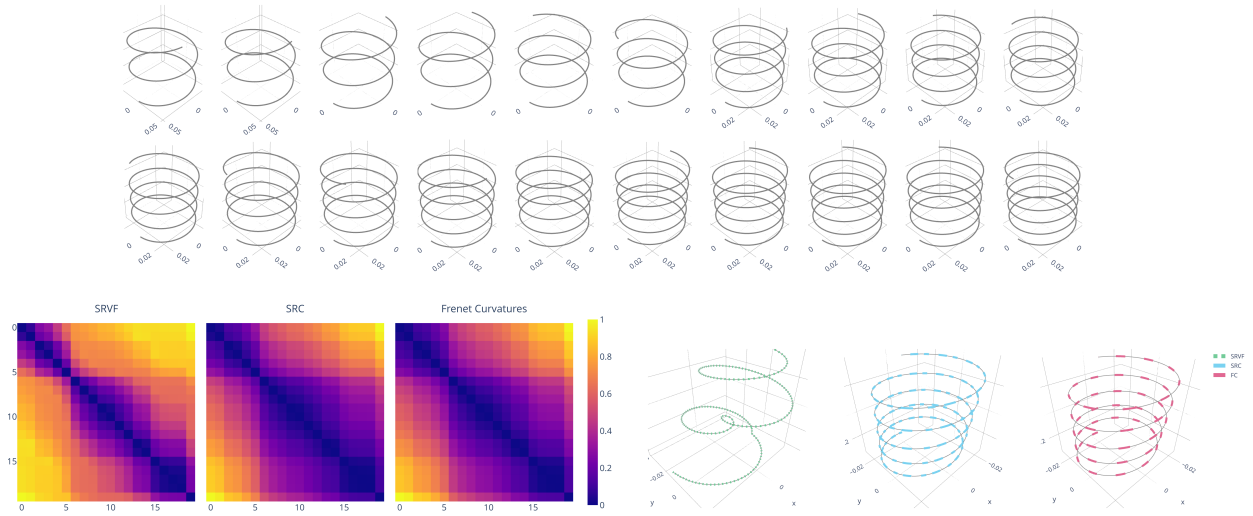

Figure S.8: Matrices of pairwise distances (right top) and Karcher means (right bottom) computed under each method (SRVF, SRC, and Frenet curvatures) from a set of 20 random circular helices plotted on the left.

3.2. Application to sign language motion data *(section 5.3 of the main article)*

We propose in section 5.3 of the main article the application of the methods for the analysis of a set of wrist movement trajectories in sign language. We consider in Figures 6 and 7 the case of the sign "Femme". In this supplementary material, we show the results obtain by doing the same analysis for another sign "Europe". Figure S.10 show the curvatures parameterized by the corresponding arc-length functions of the curves along the geodesic path between the red and blue curve visible in Figure S.9. We also observe in that case that the alignment obtains by the SRC method is more satisfying in conserving the geometry of the curves. Moreover, we see that the artefacts that appear along the SRVF geodesic path in the experiments on synthetic curves, which look like peaks of Frenet curvatures at the boundaries, are also present here. In addition, we propose by the Figure S.12 to visualize the three Karcher means of these two sets of sign trajectories.

References

[1] Nicolas J.-B. Brunel and Juhyun Park. The frenet-serret framework for aligning geometric curves. In Frank Nielsen and Frédéric Barbaresco, editors, *Geometric Science of Information*, pages 608–617, Cham, 2019. Springer International Publishing. 2

[2] Robert Lyons. Frobenius theorem two ways. *Lecture note*, 2016. 2

[3] Frank W. Warner. *Foundations of Differentiable Manifolds and Lie Groups*. 0072-5285. Springer New York, NY, 1983. 2

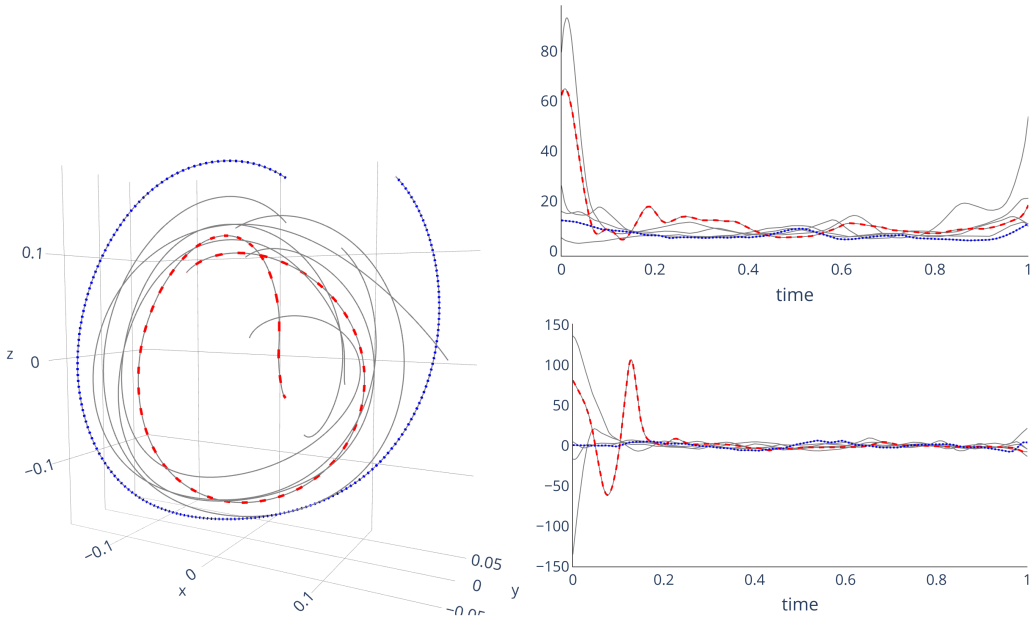

Figure S.9: Trajectories of the right wrist while signing "Europe" in sign language: 3D curves (left), time-parametrized curvatures (top right), torsions (bottom right). The blue and red ones are used to compute the geodesic in Figure S.10.

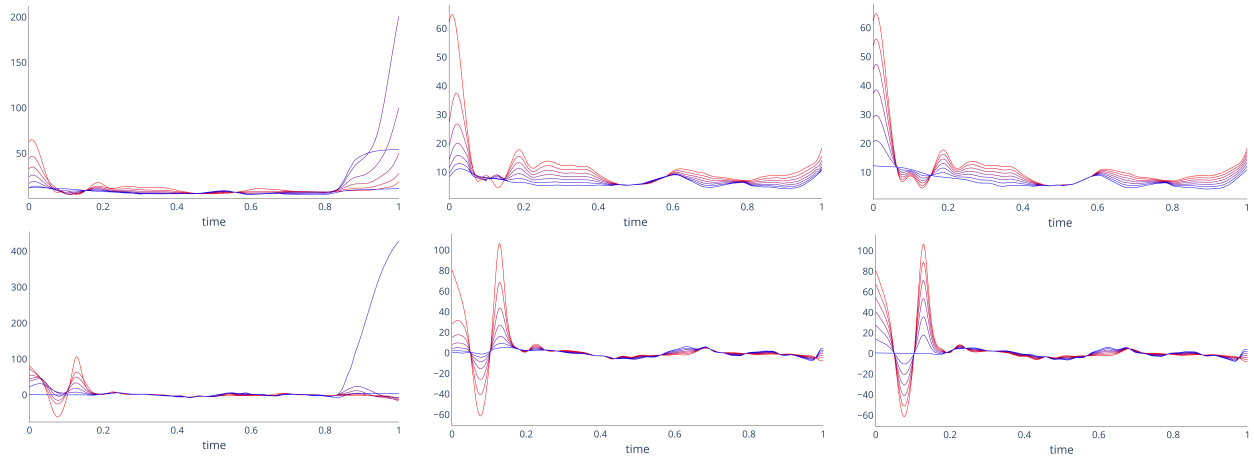

(a) SRVF (b) SRC (c) Frenet curvatures

Figure S.10: Comparison between time-parametrized curvature and torsion along the geodesic path under SRVF (left), SRC (middle), and Frenet curvatures (right).

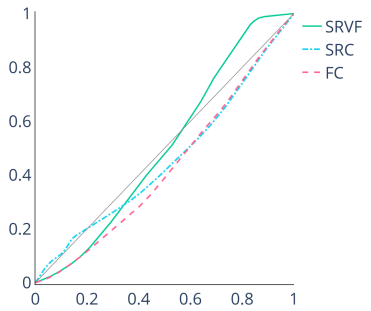

(a) Warping functions h

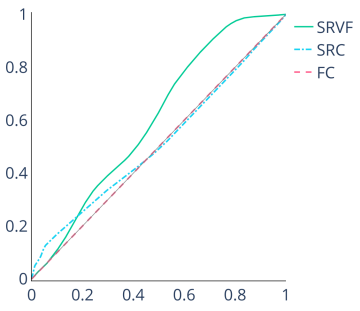

(b) Warping functions γ

Figure S.11: Comparison of estimated warping functions h (left) and γ (right) for geodesic plotted on Figure S.10.

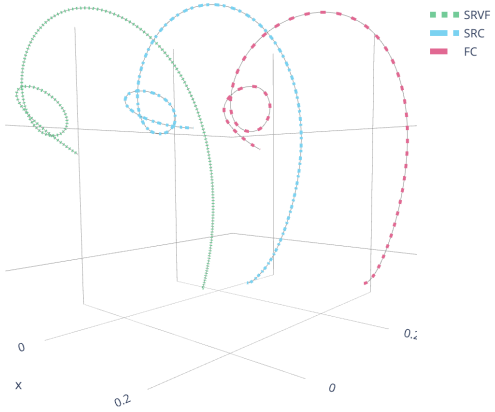

(a) Sign “Femme”

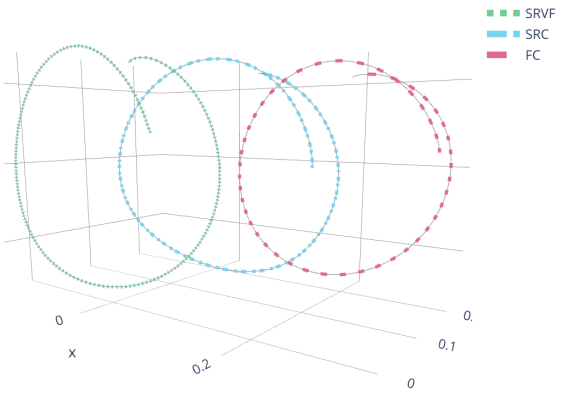

(b) Sign “Europe”

Figure S.12: Karcher means of trajectories of sign ”Femme” (left) visible in Figure 7 of the main article and sign ”Europe” (right) visible in Figure S.9, computed using the three different methods.